Quantum and classical analyses of intertwined phase transitions in odd-mass Nb isotopes

A. Leviatan,*

¹Racah Institute of Physics, The Hebrew University, Jerusalem 91904, Israel

Abstract. Quantum phase transitions (QPTs) in odd-mass Nb isotopes are investigated in the framework of the interacting boson-fermion model with configuration mixing. A quantum analysis reveals a Type I QPT (gradual shape-evolution within the intruder configuration) superimposed on a Type II QPT (abrupt crossing of normal and intruder states), thus demonstrating the occurrence of intertwined QPTs. A classical analysis highlights the implications for the single particle motion in the deformed field generated by the even-even Zr cores.

1 Introduction

Quantum phase transitions (QPTs) are qualititative changes in the properties of a physical system induced by variation of parameters in the Hamiltonian. Such structural changes are manifested empirically in nuclei as transistions between shapes and can be categorized into two types. The first, denoted as Type I [1], is a shape-phase transition within a single configuration, as encountered in the neutron number 90 region [2]. The second, denoted as Type II [3], is a phase transition involving a crossing of different configurations, as encountered in nuclei near (sub-) shell closure [4]. In most cases, the strong mixing between the configurations obscures the individual QPTs. However, if the mixing is small, the Type II QPT can be accompanied by a distinguished Type I QPT within each configuration separately. Such a scenario, referred to as intertwined QPTs, occurs in the even-even Zr (Z=40) isotopes [5-7]. In the present contribution, we discuss both quantum and classical analyses of a similar scenario in the adjacent odd-even Nb (Z=41) isotopes [8–10].

2 IBFM for multiple configurations

Odd-A nuclei are treated in the interacting boson-fermion model (IBFM) [11], as a system of monopole (s) and quadruple (d) bosons, representing valence nucleon pairs, and a single (unpaired) nucleon. The (single-configuration) IBFM Hamiltonian has the form

$$\hat{H}(\xi) = \hat{H}_{b} + \hat{H}_{f} + \hat{V}_{bf} . \tag{1}$$

We focus the discussion to an odd fermion in a single-*j* orbit for which,

$$\hat{H}_{b}(\epsilon_{d}, \kappa, \chi) = \epsilon_{d} \,\hat{n}_{d} + \kappa \,\hat{Q}_{\chi} \cdot \hat{Q}_{\chi} \tag{2a}$$

$$\hat{H}_{f}(\epsilon_{i}) = \epsilon_{i} \,\hat{n}_{i} \tag{2b}$$

$$\hat{V}_{\rm bf}(\chi,A,\Gamma,\Lambda) = A\,\hat{n}_d\,\hat{n}_j + \Gamma\,\hat{Q}_\chi\cdot(a_i^\dagger\,\tilde{a}_j)^{(2)}$$

$$+ \Lambda \, \sqrt{2j+1} : [(d^\dagger \, \tilde{a}_j)^{(j)} \times (\tilde{d} \, a_j^\dagger)^{(j)}]^{(0)} : \eqno(2\mathrm{c})$$

The boson part (2a) contains pairing and quadrupole terms, where $\hat{n}_d = \sum_m d_m^\dagger d_m$, $\hat{Q}_\chi = d^\dagger s + s^\dagger \tilde{d} + \chi \ (d^\dagger \tilde{d})^{(2)}$ and $\tilde{d}_m = (-1)^m d_{-m}$. The fermion part (2b) involves the number operator, \hat{n}_j , and the boson-fermion part (2c) is composed of monopole, quadrupole and exchange terms, where : –: denotes normal ordering and $\tilde{a}_{j,m} = (-1)^{j-m} a_{j,-m}$. A change in the parameters $\xi = (\epsilon_d, \kappa, \chi, \epsilon_j, A, \Gamma, \Lambda)$ of $\hat{H}(\xi)$ induces Type I QPTs [12–14], relevant to odd-mass nuclei.

The interacting boson-fermion model with configuration mixing (IBFM-CM) [8, 9] is an extension of the IBFM to include configurations with $N, N+2, \ldots$ bosons, representing shell model spaces built on 0p-0h, 2p-2h,... particle-hole excitations across closed shells. For two configurations (A, B), the IBFM-CM Hamiltonian can be cast in matrix form,

$$\hat{H}(\xi_A, \xi_B, \omega) = \begin{bmatrix} \hat{H}_A(\xi_A) & \hat{W}(\omega) \\ \hat{W}(\omega) & \hat{H}_B(\xi_B) \end{bmatrix} . \tag{3}$$

Here $\hat{H}_A(\xi_A)$ and $\hat{H}_B(\xi_B)$ represent, respectively, the normal A configuration (N boson space) and the intruder B configuration (N + 2 boson space), both coupled to a single j-fermion and $\hat{W}(\omega)$ a mixing term. Specifically,

$$\hat{H}_A(\xi_A) = \hat{H}_b(\epsilon_d^A, \kappa_A, \chi) + \hat{H}_f + \hat{V}_{bf} , \qquad (4a)$$

$$\hat{H}_B(\xi_B) = \hat{H}_{\rm b}(\epsilon_d^B,\kappa_B,\chi) + \kappa_B' \, \hat{L} \cdot \hat{L} + \Delta_B + \hat{H}_{\rm f} + \hat{V}_{\rm bf} \; , \eqno(4b)$$

$$\hat{W}(\omega) = \omega \left[(d^{\dagger} d^{\dagger})^{(0)} + (s^{\dagger})^2 + \text{H.c.} \right].$$
 (4c)

where $\hat{L} \cdot \hat{L}$ is a rotational term, Δ_B an energy off-set and H.c. stands for Hermitian conjugate. For simplicity, $\hat{H}_f(\epsilon_j)$ and $\hat{V}_{bf}(A,\Gamma,\lambda)$ are taken to be the same in both configurations. A change in the parameters (ξ_A,ξ_B,ω) can induce a Type I QPT within each configuration and a Type II QPT of configuration crossing. For $\hat{H}_f = \hat{V}_{bf} = 0$, the IBFM-CM Hamiltonian of Eq. (3) reduces to that of the interacting boson model with configuration mixing (IBM-CM) [15, 16], relevant to the study of configuration-mixed QPTs and shape-coexistence in even-even nuclei.

The eigenstates $|\Psi; j, J\rangle$ of \hat{H} , Eq. (3), are linear combinations of wave functions Ψ_A and Ψ_B , involving bosonic

^{*}e-mail: ami@phys.huji.ac.il

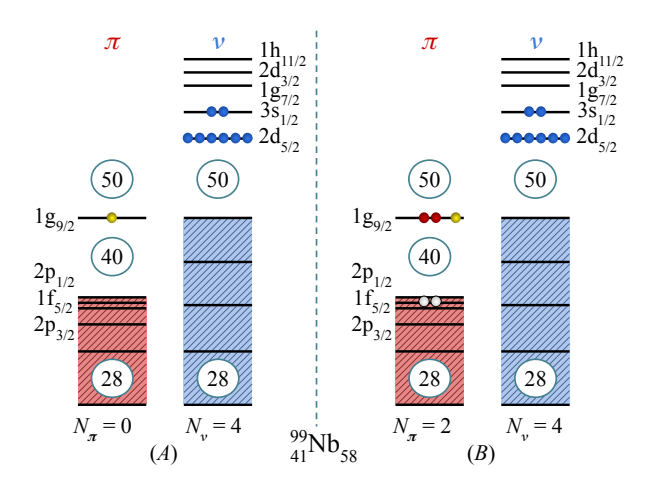


Figure 1. Schematic representation of the two coexisting shell-model configurations (A and B) for $^{99}_{41}\text{Nb}_{58}$. The corresponding numbers of proton bosons (N_π) and neutron bosons (N_ν), are listed for each configuration and $N=N_\pi+N_\nu$.

basis states in the two spaces $|[N], \alpha, L\rangle$ and $|[N+2], \alpha, L\rangle$, coupled to a *j*-fermion. The boson (L) and fermion (j) angular momenta are coupled to J,

$$\begin{split} |\Psi; j, J\rangle &= a \, |\Psi_A, [N], j; J\rangle + b \, |\Psi_B, [N+2], j; J\rangle \\ &= \sum_{\alpha, L} C_{\alpha, L, j}^{(N, J)} |N, \alpha, (L \otimes j) J\rangle \\ &+ \sum_{i} C_{\alpha, L, j}^{(N+2, J)} |N + 2, \alpha, (L \otimes j) J\rangle \,. \end{split} \tag{5}$$

The probability of normal-intruder mixing is given by,

$$a^2 = \sum_{\alpha,L} |C_{\alpha,L,j}^{(N,J)}|^2 \quad , \quad b^2 = \sum_{\alpha,L} |C_{\alpha,L,j}^{(N+2,J)}|^2 = 1 - a^2 \; . \quad (6)$$

3 Quantum analysis of the Nb chain

Positive-parity states in $_{41}^A$ Nb isotopes with mass number A=93-105 are described in the shell model by coupling a proton in a $\pi(1g_{9/2})$ orbit to the respective $_{40}$ Zr cores with neutron number 52–64. In the latter, the normal A configuration corresponds to having no active protons above the Z=40 sub-shell gap, and the intruder B configuration corresponds to two-proton excitation from below to above this gap, creating 2p-2h states. The IBFM-CM model space employed, consists of a single j=9/2 fermion and $[N] \oplus [N+2]$ boson spaces with $N=1,2,\ldots,7$ for $^{93-105}$ Nb. The two configurations relevant for 99 Nb are shown schematically in Fig. 1. The parameters of the IBFM-CM Hamiltonian (4) and transition operators are determined from a fit in the manner described in [8-10].

Figure 2 shows the experimental and calculated levels of selected states in the Nb isotopes along with assignments to configurations based on Eq. (6). Empty (filled) symbols indicate a dominantly normal (intruder) state with small (large) b^2 probability. In the region between neutron number 50 and 56, there appear to be two sets of levels

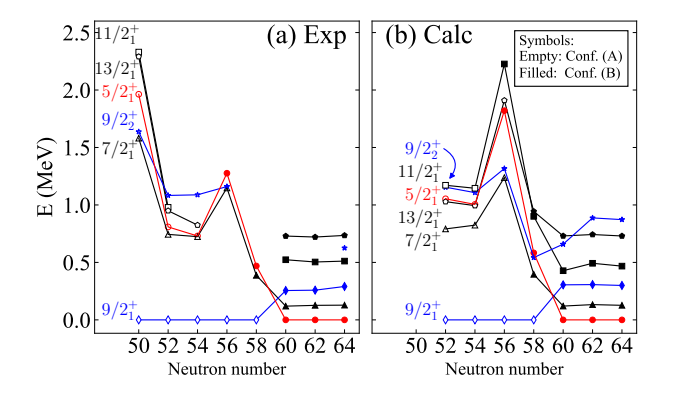
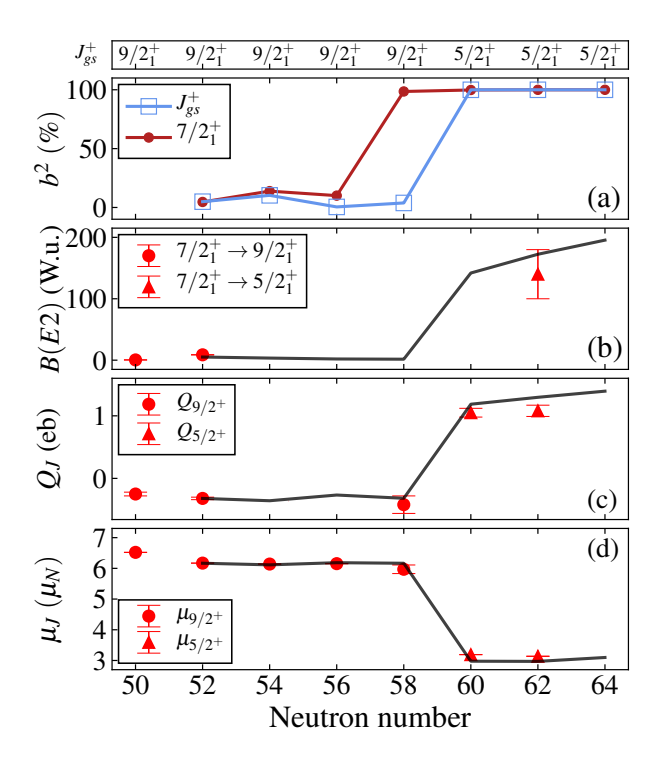


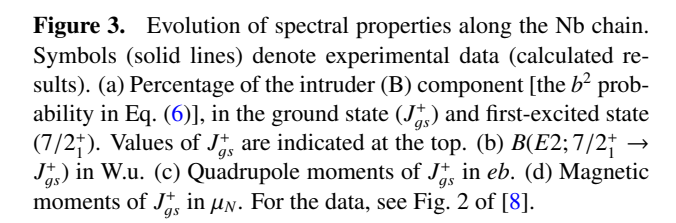
Figure 2. Comparison between (a) experimental and (b) calculated lowest-energy positive-parity levels in Nb isotopes. Empty (filled) symbols indicate a state dominated by the normal A (intruder B) configuration. In particular, the $9/2_1^+$ state is in the A (B) configuration for neutron number 52–58 (60–64) and the $5/2_1^+$ state is in the A (B) configuration for 52–54 (56–64).

with weakly deformed structure, associated with configurations A and B. All levels decrease in energy for 52–54, away from closed shell, and rise again at 56 due to the neutron $\nu(2d_{5/2})$ subshell closure. From 58, there is a pronounced drop in energy for the states of the B configuration. At 60, the two configuration cross, indicating a Type II QPT, and the ground state changes from $9/2_1^+$ to $5/2_1^+$, becoming the bandhead of a $K=5/2^+$ rotational band composed of $5/2_1^+$, $7/2_1^+$, $9/2_1^+$, $11/2_1^+$, $13/2_1^+$ states. The intruder B configuration remains strongly deformed and the band structure persists beyond 60. The above trend is similar to that encountered in the even-even Zr isotopes with the same neutron numbers (see Fig. 14 of [7]).

A possible change in the angular momentum of the ground state (J_{as}^+) is a characteristic signature of Type II QPTs in odd-mass, unlike in even-even nuclei where the ground state remains 0^+ after the crossing. It is an important measure for the quality of the calculations, since a mean-field approach, without configuration mixing, fails to reproduce the switch from $9/2_1^+$ to $5/2_1^+$ in J_{qs}^+ for the Nb isotopes [17]. Fig. 3(a) shows the percentage of the wave function within the B configuration for J_{qs}^+ and $7/2_1^+$, as a function of neutron number across the Nb chain. The rapid change in structure of J_{gs}^+ from the normal A configuration in $^{93-99}$ Nb (small b^2 probability) to the intruder B configuration in $^{101-105}$ Nb (large b^2) is clearly evident, signaling a Type II QPT. The configuration change appears sooner in the 7/2⁺ state, which changes to the B configuration already in ⁹⁹Nb. Outside a narrow region near neutron number 60, where the crossing occurs, the two configurations are weakly mixed and the states retain a high level of purity.

Further insight into the nature of the QPTs is gained by considering the behaviour of the order parameters and related observables. The $B(E2; 7/2_1^+ \rightarrow J_{gs}^+)$ and quadrupole moment of J_{gs}^+ in Nb isotopes are shown in Fig. 3(b) and Fig. 3(c), respectively. These observables are related to the deformation, the order parameter of the QPT. Although the





data is incomplete, one can still observe small (large) values of these observables below (above) neutron number 60, indicating an increase in deformation. The calculation reproduces well this trend and attributes it to a Type II QPT involving a jump between neutron number 58 and 60, from a weakly-deformed A configuration, to a stronglydeformed B configuration. Such a Type II scenario is supported also by the trend in the magnetic moments (μ_J) of the ground state, shown in 3(d), where both the data and the calculations show a constant value of μ_I for neutron numbers 52-58, and a drop to a lower value at 60, which persists for 60–64. The behavior shown in Figs. 3(b)-3(c) is correlated with a similar jump seen for the B(E2)'s of $2^+ \rightarrow 0^+$ transitions in the even-even Zr cores, Fig. 4(b), and with the calculated order parameters, Fig. 4(a). The latter are the expectation value of \hat{n}_d in the 0^+_1 ground state wave function, $\langle \hat{n}_d \rangle_{0_1^+}$, and in its normal (A) and intruder (B) components, $\langle \hat{n}_d \rangle_A$ and $\langle \hat{n}_d \rangle_B$. Their evolution along the Zr chain reveals that configuration A remains spherical, while configuration B undergoes a Type I QPT involving a gradual spherical-to-deformed [U(5)-SU(3)-SO(6)] shape-phase transition [5–7].

Additional evidence for a Type I QPT, involving shape changes within the intruder B configuration, is obtained by examining the individual structure of Nb isotopes at the end-points of the region considered. Figure 5 dis-

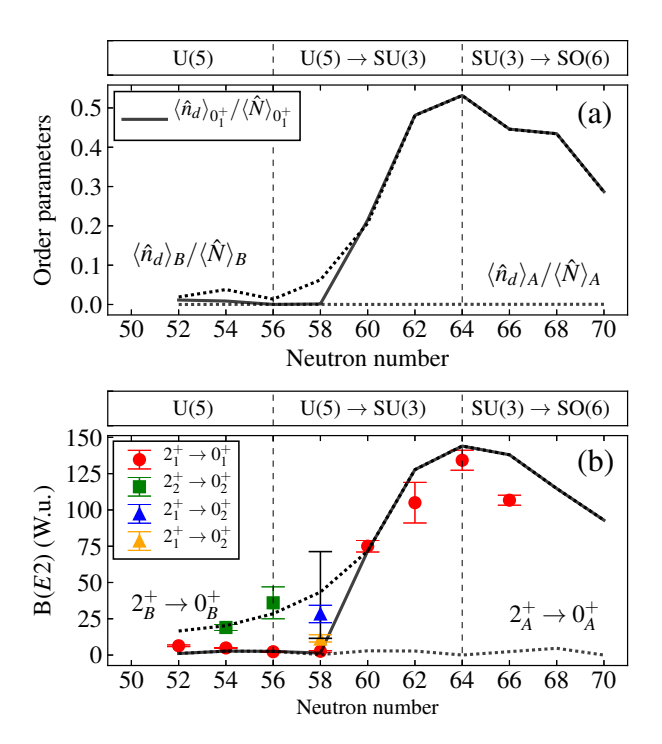


Figure 4. Evolution of spectral properties along the Zr chain. (a) Order parameters: $\langle \hat{n}_d \rangle_{0_1^+}$ (solid line) and $\langle \hat{n}_d \rangle_A$, $\langle \hat{n}_d \rangle_B$ (dotted lines), normalized by the respective boson numbers. (b) B(E2) values for $2^+ \to 0^+$ transitions in Weisskopf units (W.u.). Dotted lines denote calculated E2 rates for transitions within a configuration. Solid line denotes calculated $2^+_1 \to 0^+_1$ rates. For the data, see Fig. 17 of [7].

plays the experimental and calculated levels in 93Nb along with E2 and M1 transitions among them. The corresponding spectra of 92Zr, the even-even core, are also shown with an assignment of each level L to the normal A or intruder B configurations, based on the analysis in [7], which also showed that the two configurations in 92Zr are spherical or weakly-deformed. It has long been known that low-lying states of the A configuration in ⁹³Nb, can be interpreted in a weak coupling scheme, where the single-proton $\pi(1g_{9/2})$ state is coupled to spherical-vibrator states of the core. Specifically, for the 0_{1.4} ground state of ⁹²Zr, this coupling yields the ground state $9/2_1^+$ of 93 Nb. For $2_{1;A}^+$, it yields a quintuplet of states, $5/2_1^+, 7/2_1^+, 9/2_3^+, 11/2_1^+, 13/2_1^+,$ whose "center of gravity" (CoG), is 0.976 MeV, in agreement with the observed energy 0.935 MeV of 2_1^+ in $^{92}{\rm Zr}$. The E2 transitions from the quintuplet states to the ground state are comparable in magnitude to the $2^+_{1;A} \rightarrow 0^+_{1;A}$ transition in 92 Zr, except for $9/2^+_3$, whose decay is weaker. A nonet of states built on $4_{1:A}^+$ can also be identified in the empirical spectrum of 93 Nb, with CoG of 1.591 MeV, close to 1.495 MeV of $4_{1.4}^{+}$.

Particularly relevant to the present discussion is the fact that the weak-coupling scenario is also valid for non-yrast states of the intruder B configuration in 93 Nb. As shown in Fig. 5, the coupling of $\pi(1g_{9/2})$ to the $0_{2:B}^+$ state in

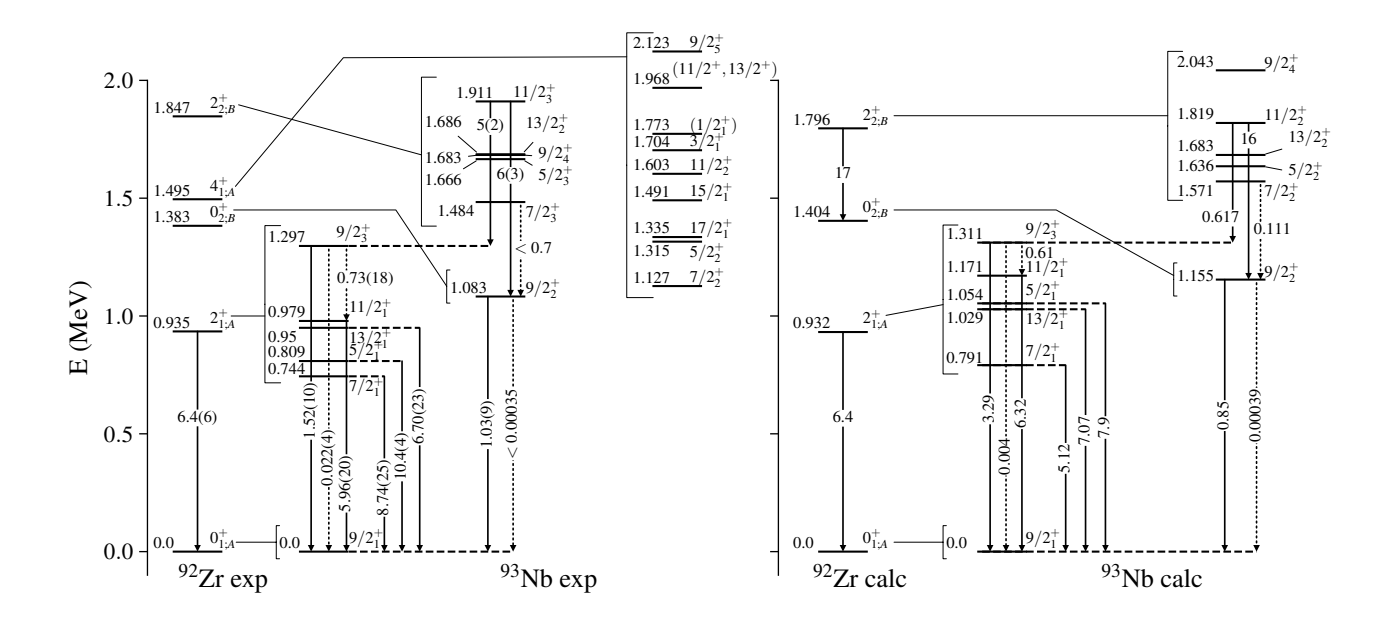


Figure 5. Experimental (left) and calculated (right) energy levels in MeV, and E2 (solid arrows) and E3 (dashed arrows) transition rates in W.u., for E3 Nb and E3 Lines connect E3 Lines conn

 92 Zr, yields the excited $9/2_2^+$ state in 93 Nb. For $2_{2:B}^+$ it yields the quintuplet, $5/2_3^+$, $7/2_3^+$, $9/2_4^+$, $11/2_3^+$, $13/2_2^+$, whose CoG is 1.705 MeV, a bit lower than 1.847 MeV of $2_{2:B}^+$. The observed E2 rates 1.03(9) W.u for $9/2_2^+ \rightarrow 9/2_1^+$, is close to the calculated value 0.85 W.u., but is smaller than the observed value 1.52(10) W.u for $9/2_3^+ \rightarrow 9/2_1^+$, suggesting that $9/2_2^+$ is associated with the B configuration.

For 103 Nb, the yrast states shown in Fig. 6 are arranged in a $K = 5/2^+$ rotational band, with an established Nilsson model assignment $5/2^+$ [422]. The band members can be interpreted in the strong coupling scheme, where a par-

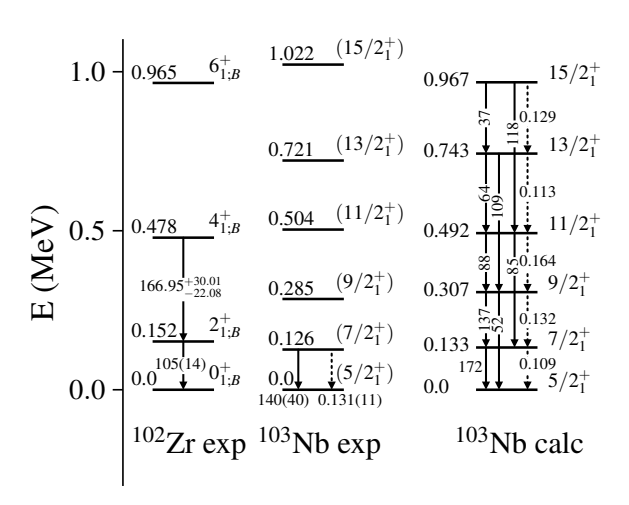


Figure 6. Experimental and calculated energy levels in MeV, and E2 (solid arrows) and M1 (dashed arrows) transition rates in W.u., for 103 Nb and 102 Zr. For the data, see Fig. 4 of [8].

ticle is coupled to an axially-deformed core. The indicated states are obtained by coupling the $\pi(1g_{9/2})$ state to the ground band ($L=0^+_{1;B},2^+_{1;B},4^+_{1;B},6^+_{1;B},\ldots$) of 102 Zr, also shown in Fig. 6, which is associated with the intruder B configuration. The calculations reproduce well the observed particle-rotor J(J+1) splitting, as well as, the E2 and M1 transitions within the band. Altogether, we see an evolution of structure from weak-coupling of a spherical shape in 93 Nb, to strong-coupling of a deformed shape in 103 Nb. Such shape-changes within the B configuration (Type I QPT), superimposed on abrupt configuration crossing (Type-II QPT), are the key defining feature of intertwined QPTs. Interestingly, this intricate scenario, originally observed in the even-even Zr isotopes [5–7], persists in the adjacent odd-even Nb isotopes.

4 Classical analysis

One of the main advantages of the algebraic approach is that one can do both a quantum and a classical analysis, thus enabling an intuitive geometric interpretation. Geometry is introduced into the IBFM by means of a matrix potential of the Hamiltonian (1) in the basis [18–20],

$$|j, m; \beta, \gamma; N\rangle = |j, m\rangle \otimes |\beta, \gamma; N\rangle$$
, (7)

which involves the product of a *j*-fermion $|j, m\rangle = a_{jm}^{\dagger}|0\rangle$ and a projective coherent state of *N* bosons [1, 21],

$$|\beta, \gamma; N\rangle = (N!)^{-1/2} (b_c^{\dagger})^N |0\rangle. \tag{8}$$

Here $b_c^{\dagger} = (1+\beta^2)^{-1/2} [\beta \cos \gamma d_0^{\dagger} + \frac{1}{\sqrt{2}}\beta \sin \gamma (d_2^{\dagger} + d_{-2}^{\dagger}) + s^{\dagger}]$ and (β, γ) are quadrupole shape variables. The resulting matrix, $\Omega_N(\beta, \gamma; \xi)$, is real and symmetric with entries $E_b(\beta, \gamma; N) \delta_{m_1, m_2} + \epsilon_j \delta_{m_1, m_2} + N g_{m_1, m_2}(\beta, \gamma)$. Here

 $E_b(\beta, \gamma; N)$ is the expectation value of \hat{H}_b (2a) in $|\beta, \gamma; N\rangle$,

$$E_{b}(\beta, \gamma; \epsilon_{d}, \kappa, \chi; N) = 5\kappa N + \frac{N\beta^{2}}{1+\beta^{2}} \left[\epsilon_{d} + \kappa(\chi^{2} - 4) \right] + \frac{N(N-1)\beta^{2}}{(1+\beta^{2})^{2}} \kappa \left[4 - 4\bar{\chi}\beta \cos 3\gamma + \bar{\chi}^{2}\beta^{2} \right], \tag{9}$$

where $\bar{\chi} = \sqrt{\frac{2}{7}}\chi$. Explicit expressions of $g_{m_1,m_2}(\beta,\gamma)$ are given in Eqs. (10)-(14) of [13]. Diagonalization of the matrix splits into two (doubly degenerate) pieces with $m = j, j - 2, \dots, -(j - 1)$ and similarly with $m \rightarrow -m$. The dimension of the basis is thus (j + 1/2). The resulting eigenvalues are the Bose-Fermi potential surfaces $E_k^{(N)}(\beta, \gamma; \xi)$, which include the contribution of the core and of the single particle levels in the deformed β and γ field generated by the bosons.

For $\gamma = 0$ (axial shape), the potential matrix $\Omega_N(\beta; \xi)$ is diagonal in the basis $|j, K; \beta; N\rangle$ with entries [18],

$$E_K^{(N)}(\beta;\xi) = E_b(\beta;N) + \epsilon_j + N\lambda_K(\beta), \qquad (10a)$$

$$\lambda_K(\beta; \chi, A, \Gamma, \Lambda) = A \frac{\beta^2}{1+\beta^2}$$

$$+\frac{\beta}{1+\beta^2}C_{jK}[\Gamma\sqrt{5}(\beta\bar{\chi}-2)-\beta\Lambda(2j+1)C_{jK}],$$
 (10b)

where $C_{jK} = \frac{3K^2 - j(j+1)}{\sqrt{(2j-1)(2j+1)(2j+3)j(j+1)}}$. The dependence of $\lambda_K(\beta)$ on K^2 reflects the double degeneracy $(K \to -K)$ mentioned above.

A geometric interpretation for the IBFM-CM [10, 22], is obtained by constructing from the Hamiltonian (3) an enlarged potential matrix of order $(2j + 1) \times (2j + 1)$, in the basis $\{|j, m_1; \beta, \gamma; N\rangle, |j, m_2; \beta, \gamma; N+2\rangle\}$, with $m_1, m_2 =$ $j, j - 2, \ldots, -(j-1),$

$$\Omega_N(y;\xi_A,\xi_B,\omega) = \left[\begin{array}{c|c} \Omega_A(y;\xi_A) & \Omega_{AB}(y;\omega) \\ \hline \Omega_{AB}(y;\omega) & \Omega_B(y;\xi_B) \end{array} \right] . \tag{11}$$

The matrix depends on $y \equiv (\beta, \gamma)$ and on the parameters of the Hamiltonian, Eq. (4), $\xi_A = (\epsilon_d^A, \kappa_A, \chi, \epsilon_j^A, A, \Gamma, \Lambda), \xi_B =$ $(\epsilon_d^B, \kappa_B, \chi, \kappa_B', \Delta_B, \epsilon_i^B, A, \Gamma, \Lambda), \omega \text{ and } N.$ The sub-matrix $\Omega_A(\beta, \gamma; \xi_A)$ acts in the $|j, m_1; y; N\rangle$ sector, $\Omega_B(\beta, \gamma; \xi_B)$ acts in the $|j, m_2; y; N + 2\rangle$ sector and $\Omega_{AB}(\beta, \gamma; \omega)$ connects the two sectors. For $\hat{H}_f = \hat{V}_{bf} = 0$, the above potential matrix reduces to that proposed for the IBM-CM [23]. Diagonalization of the matrix $\Omega_N(y; \xi_A, \xi_B, \omega)$ produces the

For $\gamma = 0$, the matrix $\Omega_N(\beta; \xi_A, \xi_B, \omega)$ of Eq. (11), can be transformed into a simple block-diagonal form $\{M_{K=j}(\beta), M_{K=j-2}(\beta), \ldots, M_{K=-(j-1)}(\beta)\}, \text{ where } M_K(\beta)$ stands for a 2 × 2 matrix in the states $|\Psi_{A;K}\rangle \equiv |j,K;\beta;N\rangle$ and $|\Psi_{B;K}\rangle \equiv |j,K;\beta;N+2\rangle$

$$M_K(\beta) = \begin{bmatrix} E_{A;K}(\beta) & W(\beta) \\ W(\beta) & E_{B;K}(\beta) \end{bmatrix}. \tag{12}$$

Using Eq. (10), the entries of $M_K(\beta)$ are given by,

$$E_{A;K}(\beta) = E_K^{(N)}(\beta; \xi_A) ,$$
 (13a)

$$E_{B;K}(\beta) = E_K^{(N+2)}(\beta; \xi_B) + 6\kappa_B' \frac{(N+2)\beta^2}{1+\beta^2} + \Delta_B , \qquad (13b)$$

$$W(\beta) = \frac{\sqrt{(N+2)(N+1)}}{1+\beta^2} \omega \left(1 + \frac{1}{\sqrt{5}}\beta^2\right). \tag{13c}$$

Introducing the quantities,

$$\delta_K(\beta) = E_{B:K}(\beta) - E_{A:K}(\beta) , \qquad (14a)$$

$$R_K(\beta) = \frac{\delta_K(\beta)}{2W(\beta)}, \qquad (14b)$$

the eigen-potentials then read,

$$E_{\pm,K}(\beta) = \frac{1}{2} \Sigma_K(\beta) \pm \left| W(\beta) \right| \sqrt{1 + [R_K(\beta)]^2} , \qquad (15)$$

where $\Sigma_K(\beta) = E_{A:K}(\beta) + E_{B:K}(\beta)$, and the corresponding eigenvectors are

$$|\Psi_{-,K}(\beta)\rangle = a|\Psi_{A;K}\rangle + b|\Psi_{B;K}\rangle,$$
 (16a)

$$|\Psi_{+,K}(\beta)\rangle = -b |\Psi_{A;K}\rangle + a |\Psi_{B;K}\rangle.$$
 (16b)

The ratio of mixing amplitudes and probabilities satisfy,

$$\frac{b}{a} = \left[R_K(\beta) \mp \sqrt{1 + [R_K(\beta)]^2} \right], \tag{17a}$$

$$\frac{b}{a} = \left[R_K(\beta) \mp \sqrt{1 + [R_K(\beta)]^2} \right],$$
(17a)
$$b^2 = 1 - a^2 = \frac{1}{1 + \left[R_K(\beta) \pm \sqrt{1 + [R_K(\beta)]^2} \right]^2},$$
(17b)

where the upper (lower) sign applies for $W(\beta) > 0$ $[W(\beta) < 0].$

The ensemble of eigen-potentials $\{E_{-,K}(\beta), E_{+,K}(\beta)\}\$, Eq. (15), portray the change in energies of the odd fermion as a function of deformation β , in the presence of coupled bosonic cores. The states $\{\Psi_{-,K}(\beta), \Psi_{+,K}(\beta)\}\$, Eq. (16), depict the change in configuration content. The value of $R_K(\beta)$, Eq. (14b), determines the character of the normalintruder mixing. We observe maximal mixing for $R_K(\beta)$ = 0, strong mixing for $|R_K(\beta)| \ll 1$, weak mixing for $|R_K(\beta)| >> 1$ and no mixing for $|R_K(\beta)| = \infty$.

Two scenarios are relevant for the subsequent discussion. (a) Maximal mixing occurs for $\delta_K(\beta) = 0$, i.e., when the two unmixed surfaces are degenerate, $E_{A:K}(\beta) =$ $E_{B;K}(\beta) \equiv E_K^{(0)}(\beta)$. In this case, the eigen-potentials are $E_{\pm}(\beta) = E_K^{(0)}(\beta) \pm |W(\beta)|$ and the corresponding eigenfunctions, Eq. (16), have $\frac{b}{a} = +1$ (-1) for $W(\beta) < 0$ $[W(\beta) > 0]$. (b) No mixing occurs for $W(\beta) = 0$. In this case, for $\delta_K(\beta) > 0$: $E_{-,K}(\beta) = E_{A,K}(\beta)$, $|\Psi_{-,K}\rangle =$ $|\Psi_{A;K}\rangle$, $E_{+,K}(\beta) = E_{B;K}(\beta)$, $|\Psi_{+,K}\rangle = |\Psi_{B;K}\rangle$. In contrast, for $\delta_K(\beta)$ < 0: $E_{-,K}(\beta) = E_{B;K}(\beta)$, $|\Psi_{-,K}\rangle = |\Psi_{B;K}\rangle$, $E_{+,K}(\beta) = E_{A;K}(\beta), |\Psi_{+,K}\rangle = -|\Psi_{A,K}\rangle$. In what follows, we apply the formalism to interpret geometrically the results of the quantum analysis in Section 3 for odd-mass Nb isotopes [10].

Intertwined QPTs are characterized by a weak coupling [small $W(\beta)$, Eq. (13c)] and a rapid crossing of the two configurations. At the crossing point $[\delta_K(\beta) = 0]$, Eq. (14a)], the mixing in $|\Psi_{\pm,K}\rangle$, Eq. (16), is maximal. The crossing of $E_{A;K}(\beta)$ and $E_{B;K}(\beta)$ implies a change in sign of $\delta_K(\beta)$, and the two eigenfunctions $\{\Psi_{-,K}, \Psi_{+,K}\}$ interchange their character. Away from the crossing point, the system rapidly converges to the no-mixing scenario mentioned above.

Figures 7-8 show for each K the unmixed surfaces, $E_{A,B;K} \equiv \{E_{A;K}(\beta), E_{B;K}(\beta)\}\$ (left panels) and the lowest eigen-potentials, $E_{-,K}(\beta)$ (middle panels) which serve as the Landau potentials for the Nb isotopes considered. Also shown are the purely bosonic surfaces $\{E_{b,A}(\beta), E_{b,B}(\beta)\}\$, and $E_{b,-}(\beta)$, obtained by taking $\hat{H}_f = \hat{V}_{bf} = 0$ in the Hamiltonian (4). The contour plots $E_{b,-}(\beta, \gamma)$ (right panels) are the lowest eigen-potentials of the adjacent even-even Zr cores. The latter classical potentials confirm the quantum results [5-7], as they show a transition from spherical

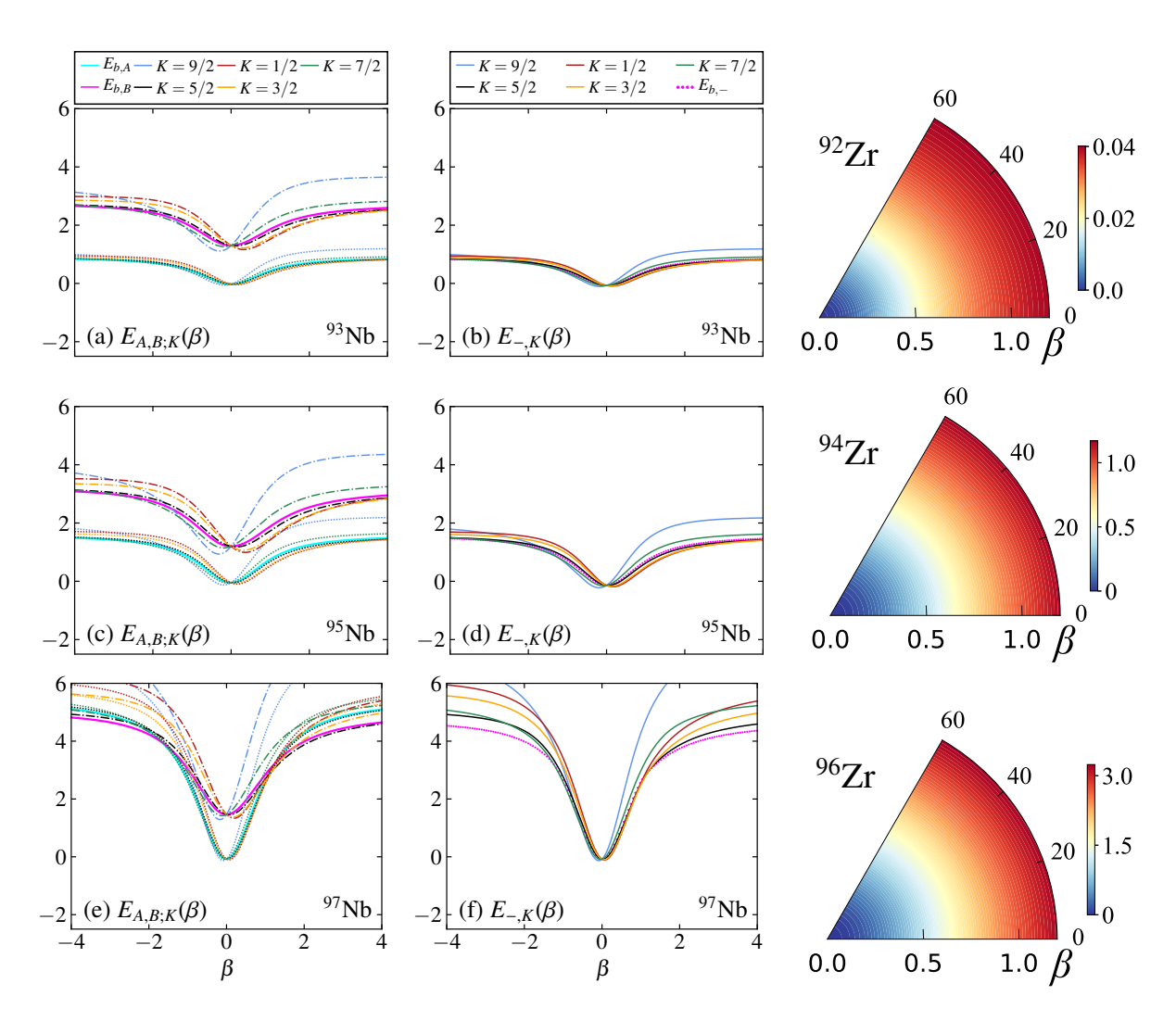


Figure 7. Unmixed surfaces $E_{A,B;K} = \{E_{A;K}(\beta), E_{B;K}(\beta)\}$, Eqs. (13a)-(13b), (left panels) and eigen-potentials $E_{-,K}(\beta)$, Eq. (15), (middle panels) in MeV for ^{93,95,97}Nb. Purely bosonic surfaces are also shown. Contour plots of eigen-potentials, $E_{-,K}(\beta, \gamma)$, for ^{92,94,96}Zr (right panels).

 $(^{92-98}\mathrm{Zr})$, to a flat-bottomed potential at $^{100}\mathrm{Zr}$, and to a prolate axially-deformed ($^{102}\mathrm{Zr}$). For $\beta=0$, the unmixed surfaces, $E_{A,B;K}(\beta)$, are independent of K. For $\beta\neq0$, they exhibit quadratic and quartic K-splitting, Eq. (10b). The resulting landscape is asymmetric in β and is identical to that encountered in the IBFM with a single configuration [18]. As discussed below, the presence or absence of crossing of the unmixed surfaces, has a direct impact on the topology of the eigen-potentials $E_{\pm,K}(\beta)$, Eq. (15).

In 93,95 Nb, we see from Figs. 7(a) and 7(c), that $\delta_K(\beta) > 0$ for all values of β , hence for each K, $E_{A;K}(\beta)$ and $E_{B;K}(\beta)$, are well separated and do not intersect. Consequently, the eigen-potentials, shown in Figs. 7(b) and 7(d), are similar to the unmixed surfaces, $E_{-,K}(\beta) \approx E_{A;K}(\beta)$, $E_{+,K}(\beta) \approx E_{B;K}(\beta)$.

In 93 Nb, all K-surfaces $E_{-,K}(\beta)$ of Fig. 7(b), are close in energy and are similar to the boson surface, $E_{b,-}(\beta)$, with a minimum at $\beta = 0$. This behavior reflects a spherical core shape weakly coupled to a j-fermion, consistent with the quantum analysis of Section 3. The latter as-

signs a weak-coupling type of wave function $|(L \otimes j)J\rangle$ with L=0, j=J=9/2, to the normal ground state [8, 9].

In 95 Nb, $E_{-,K}(\beta)$ of Fig. 7(d), display similar topology but are more dispersed. For small β , the observed K-splitting is linear in β and quadratic in K, in accord with Eq. (10b). The factor $C_{jK} \propto [3K^2 - j(j+1)]$ implies opposite shifts for K = 1/2, 3/2, 5/2 and K = 7/2, 9/2 levels, with respect to the boson surface $E_{\rm b,-}(\beta)$.

In 97,99,101,103 Nb, we see from Figs. 7(e), 8(a), 8(c), 8(e), the occurrence of regions in β with different signs for $\delta_K(\beta)$, Eq. (14a), due to crossing of the unmixed surfaces. The crossing points are on the prolate side at $\beta_K^* > 0$ and on the oblate side at $\beta_K^{**} < 0$. At these points, $\delta_K(\beta_K^*) = \delta_K(\beta_K^{**}) = 0$ and $|\Psi_{\pm,K}\rangle$, Eq. (16), exhibit maximal mixing. β_K^{**} and β_K^* mark the borders of regions with alternating sign of $\delta_K(\beta)$. I) $\beta < \beta_K^{**}$ ($\delta_K(\beta) < 0$); II) $\beta_K^{**} < \beta < \beta_K^*$ ($\delta_K(\beta) > 0$); III) $\beta > \beta_K^*$ ($\delta_K(\beta) < 0$). Region II includes $\beta = 0$. As the system evolves from one region to adjacent one, the two eigen-potentials switch their configuration-content ($A \leftrightarrow B$). Specifically, in regions I and III, we find $E_{-K}(\beta) \approx E_{B;K}(\beta)$ and $E_{+K}(\beta) \approx E_{A;K}(\beta)$,

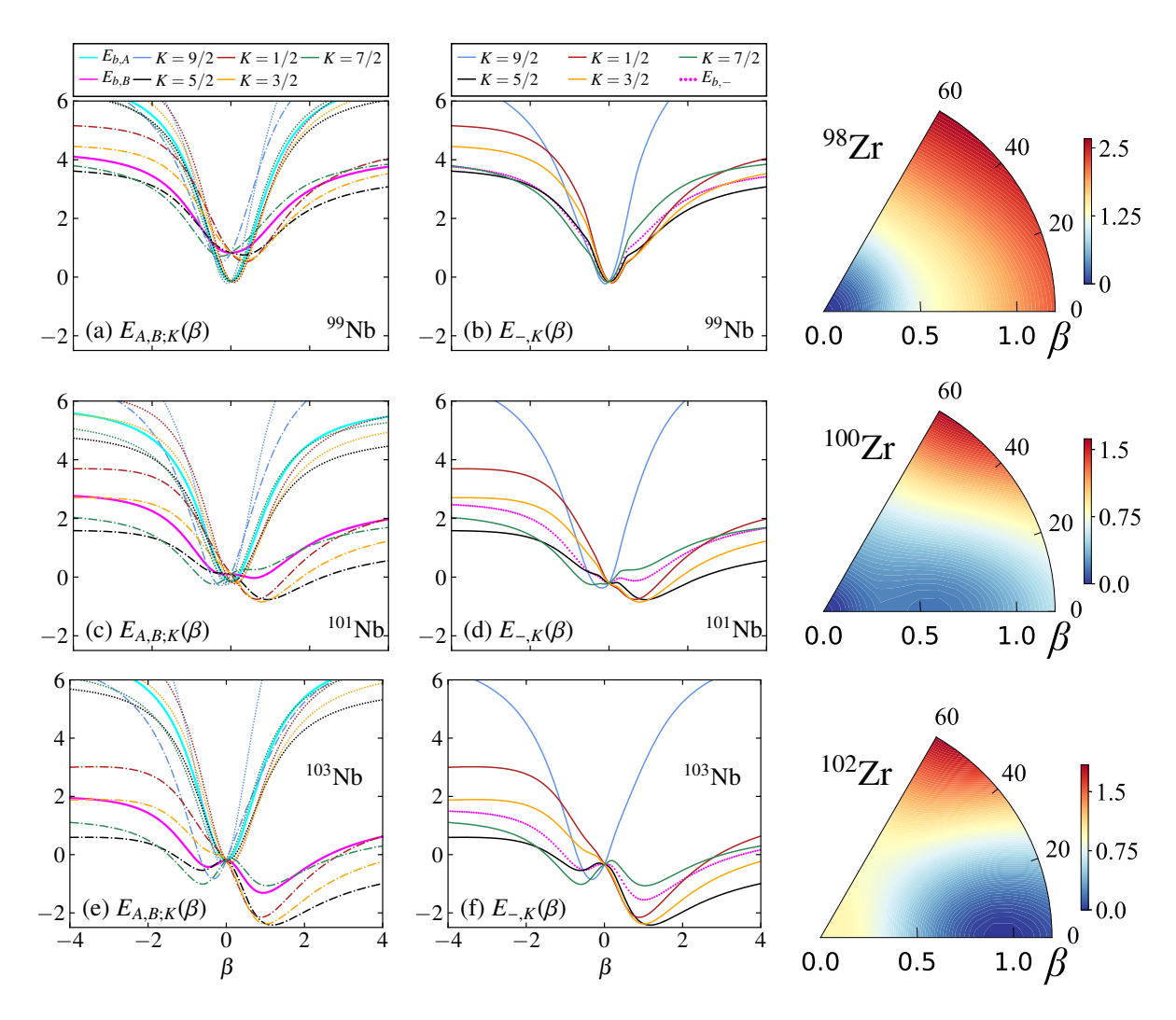


Figure 8. Unmixed surfaces $E_{A,B,K} \equiv \{E_{A;K}(\beta), E_{B;K}(\beta)\}$, Eqs. (13a)-(13b), (left panels) and eigen-potentials $E_{-,K}(\beta)$, Eq. (15), (middle panels) in MeV for 99,101,103 Nb. Purely bosonic surfaces are also shown. Contour plots of eigen-potentials, $E_{-,K}(\beta, \gamma)$, for 98,100,102 Zr (right panels).

while in region II, $E_{-,K}(\beta) \approx E_{A;K}(\beta)$ and $E_{+,K}(\beta) \approx E_{B;K}(\beta)$.

In ⁹⁷Nb, the crossing of $E_{A;K}(\beta)$ and $E_{B;K}(\beta)$, shown in Fig. 7(e), occurs at high energies and their slopes at the crossing points $(\beta_K^*$ and $\beta_K^{**})$ are similar. Consequently, these crossings have little effect on the eigen-potentials, shown in Fig. 7(f). In particular, the minimum of $E_{-K}(\beta)$ remains at $\beta = 0$, and in its vicinity $E_{-K}(\beta) \approx E_{A;K}(\beta)$.

In ⁹⁹Nb, the crossing of unmixed surfaces, shown in Fig. 8(a), occurs at lower energies, and their slopes at the crossing points are different. This leads to "kinks" in the eigen-potentials of Fig. 8(b). Particularly noticeable are the kinks in the $K=1/2,\,3/2,\,5/2$ levels, exhibiting a downward bend in $E_{-,K}(\beta)$ on the prolate side. Such kinks signal the approach to the critical point of the Type II QPT at neutron number 60, where the ground state changes from the normal (A) to the intruder (B) configuration. The minimum of $E_{-,K}(\beta) \approx E_{A;K}(\beta)$ is still at $\beta=0$.

The crossing points $\beta_K^* > 0$ and $\beta_K^{**} < 0$ of the unmixed surfaces approach each other as the mass number increases. Consequently, region II shrinks and in

the heavier 101,103 Nb isotopes, the eigen-potentials satisfy $E_{-,K}(\beta) \approx E_{B;K}(\beta)$ for most values of β .

In 101 Nb, the $E_{-,K}(\beta)$ surfaces with K = 1/2, 3/2, 5/2, develop prolate-deformed minima in region III, reflecting a transition to rotational-band structure of intruder K-bands. As seen in Fig. 8(d), these deformed minima are deeper than the shallow minimum in the flat-bottomed boson surface $E_{\rm b,-}(\beta)$ of 100 Zr, and occur at different locations. This highlights the effect of the odd fermion on the QPT in the vicinity of the critical point.

In ¹⁰³Nb, all surfaces satisfy $E_{-,K}(\beta) \approx E_{B;K}(\beta)$ and support pronounced prolate-deformed minima (except for K=9/2), upon which rotational K-bands of intruder states are built. The lowest bandhead in Fig. 8(f) has K=5/2, in line with the quantum analysis of Section 3. The latter assigns a strong coupling type of wave function to members of the ground band [8, 9]. The surfaces $E_{-,K}(\beta)$ with K=5/2,7/2, support also oblate-deformed local minima.

The equilibrium deformations obtained from the global minimum of the unmixed surfaces and lowest eigen-potential, $\beta_{eq}(E_{A;K})$, $\beta_{eq}(E_{B;K})$ and $\beta_{eq}(E_{-,K})$, serve

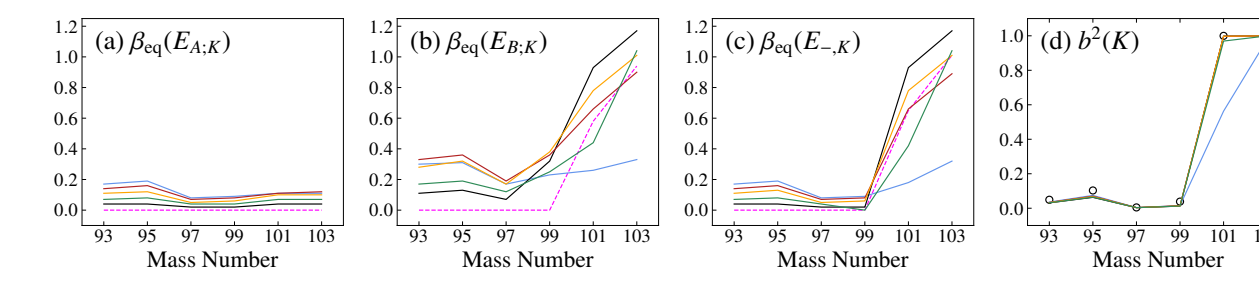


Figure 9. Equilibrium deformations (absolute value) of the unmixed surfaces (a) $\beta_{eq}(E_{A;K})$ and (b) $\beta_{eq}(E_{B;K})$, and of the lowest eigenpotential (c) $\beta_{eq}(E_{-,K})$. Dashed lines denote the minima, $\beta_{eq}(E_{b,A})$, $\beta_{eq}(E_{b,B})$, $\beta_{eq}(E_{b,-})$, of the corresponding purely bosonic surfaces. (d) Probability $b^2(K)$, Eq. (17b), of the intruder component in $|\Psi_{-K}(\beta)\rangle$ at $\beta_{eq}(E_{-,K})$. Open circles (o) denote $b^2(J_{gs}^+)$ for the ground state in the quantum analysis [8, 9], where $J_{gs}^+ = 9/2^+$ (5/2+) for 93,95,97,99 Nb (101,103 Nb). Color coding for different K values as in Figs. 7-8.

as order parameters of the QPT. Their evolution along the Nb chain is shown in Fig. 9(a), 9(b), 9(c), along with $\beta_{\rm eq}(E_{b,A}),\,\beta_{\rm eq}(E_{b,B}),\,\beta_{\rm eq}(E_{b,-})$ of the corresponding boson surfaces. (For $^{101}{\rm Nb},\,E_{b,-}(\beta)$ exhibits close-in-energy spherical and deformed minima). The normal A configuration remains spherical along the Nb chain $(\beta_{\rm eq}(E_{A;K})<0.2),$ while the intruder B configuration changes gradually from weakly deformed in $^{93}{\rm Nb}$ $(\beta_{\rm eq}(E_{B;K})\approx0.3-0.4)$ to strongly deformed in $^{103}{\rm Nb}$ $(\beta_{\rm eq}(E_{B;K})\approx0.9-1.2$ (except for K=9/2). $\beta_{\rm eq}(E_{-,K})$ is similar to $\beta_{\rm eq}(E_A)$ for $^{93,95,97,99}{\rm Nb}$ and coincides with $\beta_{\rm eq}(E_{B;K})$ for $^{101,103}{\rm Nb}.$

Fig. 9(d) shows the probability $b^2(K)$ of the intruder component in the eigenvector $|\Psi_{-K}\rangle$, Eq. (16a) at $\beta_{\rm eq}(E_{-K})$, along the Nb chain. The rapid change in structure from the normal A configuration in $^{93-99}{\rm Nb}$ (small b^2) to the intruder B configuration in $^{101,103}{\rm Nb}$ (large b^2) is clearly evident. The values of $b^2(K)$ calculated from Eq. (17b), agree with the exact values of $b^2(J_{\rm gs}^+)$ in the ground state, obtained from Eq. (6) and shown in Fig. 3(a). The combined results of Fig. 9 confirm the scenario of intertwined QPTs in the odd-mass Nb isotopes.

5 Concluding remarks

We have investigated the evolution of structure in odd-mass Nb isotopes in the framework of the IBFM-CM. A quantum analysis discloses the effects on spectral properties of an abrupt crossing of normal and intruder states (Type II QPT) accompanied by a gradual evolution from spherical- to deformed-core shapes and transition from weak to strong coupling within the intruder configuration (Type I QPT). The pronounced presence of both types of QPTs demonstrates the occurrence of intertwined QPTs in these odd-mass nuclei. A classical analysis, based on an extended matrix coherent states formalism, clarifies the effects of deformation and configuration-mixing on the single particle motion, and captures essential features of the quantum results.

A fruitful collaboration with N. Gavrielov (HU) and F. Iachello (Yale) on the topics considered, is acknowledged.

References

[1] A.E.L. Dieperink, O. Scholten, F. Iachello, Phys. Rev. Lett. **44**, 1747 (1980).

- [2] P. Cejnar, J. Jolie, R. F. Casten, Rev. Mod. Phys. **82**, 2155 (2010).
- [3] A. Frank, P. Van Isacker, F. Iachello, Phys. Rev. C **73**, 061302(R) (2006).
- [4] K. Heyde, J. L. Wood, Rev. Mod. Phys. **83**, 1467 (2011).
- [5] N. Gavrielov, A. Leviatan, F. Iachello, Phys. Rev. C 99, 064324 (2019).
- [6] N. Gavrielov, A. Leviatan, F. Iachello, Phys. Scr. 95, 024001 (2020).
- [7] N. Gavrielov, A. Leviatan, F. Iachello, Phys. Rev. C 105, 014305 (2022).
- [8] N. Gavrielov, A. Leviatan, F. Iachello, Phys. Rev. C 106, L051304 (2022).
- [9] N. Gavrielov, Phys. Rev. C 108, 014320 (2023).
- [10] A. Leviatan, N. Gavrielov, Phys. Lett. B 868, 139647 (2025).
- [11] F. Iachello, P. Van Isacker, *The Interacting Boson-Fermion Model*, (Cambridge Univ. Press, 1991).
- [12] F. Iachello, A. Leviatan, D. Petrellis, Phys. Lett. B **705**, 379 (2011).
- [13] D. Petrellis, A. Leviatan, F. Iachello, Ann. Phys. 326, 926 (2011).
- [14] M. Böyükata, C.E. Alonso, J.M. Arias, L. Fortunato, A. Vitturi, Symmetry 13, 215 (2021).
- [15] P. D. Duval, B. R. Barrett, Phys. Lett. B **100**, 223 (1981).
- [16] P. D. Duval, B. R. Barrett, Nucl. Phys. A 376, 213 (1982).
- [17] R. Rodríguez-Guzmán, P. Sarriguren, L. M. Robledo, Phys. Rev. C 83, 044307 (2011).
- [18] A. Leviatan, Phys. Lett. B 209, 415 (1988).
- [19] A. Leviatan, B. Shao, Phys. Rev. Lett. 63, 2204 (1989).
- [20] C.E. Alonso, J.M. Arias, F. Iachello, A. Vitturi, Nucl. Phys. A 539, 59 (1992).
- [21] J. N. Ginocchio, M. W. Kirson, Phys. Rev. Lett. 44, 1744 (1980).
- [22] E. Maya-Barbecho, J. E. García-Ramos, Phys. Lett. B 868, 139724 (2025).
- [23] A. Frank, P. Van Isacker, C. E. Vargas, Phys. Rev. C 69, 034323(R) (2004).